Bioinorganic Electrochemistry

Bioinorganic Electrochemistry

Edited by

Ole Hammerich
University of Copenhagen, Denmark

and

Jens Ulstrup
Technical University of Denmark

Springer

A C.I.P. Catalogue record for this book is available from the Library of Congress.

ISBN 978-1-4020-6499-9 (HB)
ISBN 978-1-4020-6500-2 (e-book)

Published by Springer,
P.O. Box 17, 3300 AA Dordrecht, The Netherlands.

www.springer.com

Printed on acid-free paper

Contents

Contributing Authors

Tim Albrecht
Department of Chemistry and NanoDTU, Building 207, Technical University of Denmark, Kemitorvet, DK-2800 Kgs. Lyngby, Denmark

Fraser A. Armstrong
Department of Chemistry, Inorganic Chemistry Laboratory, University of Oxford, Oxford, OX1 3QR, UK.

Julea N. Butt
Centre for Metalloprotein Spectroscopy and Biology, School of Chemical Sciences and Pharmacy, University of East Anglia, Norwich, NR4 7TJ, UK.

Qijin Chi
Department of Chemistry and NanoDTU, Building 207, Technical University of Denmark, Kemitorvet, DK-2800 Kgs. Lyngby, Denmark

Alexander R. Dunn
Beckman Institute, MC 139-74, California Institute of Technology, Pasadena, California 91125, USA.

David G. Fernig
The School of Biological Sciences and The Centre for Nanoscale Science, Chemistry Department, University of Liverpool, Liverpool, L69 7ZB, UK.

Harry B. Gray
Beckman Institute, MC 139-74, California Institute of Technology, Pasadena, California 91125, USA.

Wolfgang Haiss
Centre for Nanoscale Science, Chemistry Department, University of Liverpool, Liverpool, L69 7ZD, UK.

Corinna R. Hess
Beckman Institute, MC 139-74, California Institute of Technology, Pasadena, California 91125, USA.

Michael G. Hill
Occidental College, Department of Chemistry, Los Angeles, CA 90041, USA.

Shana O. Kelley
Boston College, Eugene F. Merkert Chemistry Center, Chestnut Hill, MA 02467, USA.

Alexander M. Kuznetsov
The A.N. Frumkin Institute of Physical Chemistry and Electrochemistry of the Russian Academy of Sciences, Leninskij Prospect 31, 119071 Moscow, Russia

Richard J. Nichols
Centre for Nanoscale Science, Chemistry Department, University of Liverpool, Liverpool, L69 7ZD, UK.

David J. Schiffrin
Centre for Nanoscale Science, Chemistry Department, University of Liverpool, Liverpool, L69 7ZD, UK.

Jens Ulstrup
Department of Chemistry and NanoDTU, Building 207, Technical University of Denmark, Kemitorvet, DK-2800 Kgs. Lyngby, Denmark.

Mårten Wikström
Helsinki Bioenergetics Group, Institute of Biotechnology, University of Helsinki, PB 65, 00014 University of Helsinki, Finland.

Bilha Willner
Institute of Chemistry, The Hebrew University of Jerusalem, Jerusalem 91904, Israel.

Itamar Willner
Institute of Chemistry, The Hebrew University of Jerusalem, Jerusalem 91904, Israel.

Jay R. Winkler
Beckman Institute, MC 139-74, California Institute of Technology, Pasadena, California 91125, USA.

Harm Van Zalinge
Centre for Nanoscale Science, Chemistry Department, University of Liverpool, Liverpool, L69 7ZD, UK.

Jingdong Zhang
Department of Chemistry and NanoDTU, Building 207, Technical University of Denmark, Kemitorvet, DK-2800 Kgs. Lyngby, Denmark.

Preface

Interfacial electrochemistry of redox metalloproteins and DNA-based molecules is presently moving towards new levels of structural and functional resolution. Underlying fundamentals of electron and proton transfer are increasingly well understood although also with new challenges relating to the composite interfacial solid-electrolyte environment. The new inorganic bioelectrochemistry draws further from comprehensive studies of the interfacial environments for retaining biological charge transfer function of these highly sensitive macromolecular systems. Other biotechnology has been the use of mutant proteins, DNA-base variability and *de novo* synthetic metalloproteins.

Physical electrochemistry underwent a remarkable evolution from the 1970's, almost to be likened by a renaissance and prompted by close interaction between electrochemistry and surface physics. The introduction of single-crystal atomically planar electrode surfaces was a major breakthrough and laid the foundation for other new technology such as spectroscopic techniques and statistical mechanical and electronic structure theories. Only slightly later scanning tunneling (STM) and atomic force microscopy (AFM) signalled a lift of interfacial electrochemistry to unprecedented structural resolution. Atomic resolution of pure metal and semiconductor electrode surfaces and at least sub-molecular resolution of electrochemical adsorbates could be achieved, opening new worlds of microscopic structures and processes.

Similar boundary-traversing efforts are now visible in interfacial electrochemistry of proteins and DNA-based molecules. This has led to

improved voltammetric sensitivity and structural mapping of the bioelectrochemical solid-liquid interface to single-molecule resolution. It is in fact remarkable that molecules as large and fragile as redox metalloproteins adsorbed on electrode surfaces can be mapped in their functional state by a subtle physical phenomenon, the quantum mechanical tunneling effect. These openings have offered new theoretical challenges for electron tunneling through biological macromolecules, the role of the metal centres, and the finite-size stochastic nature of the systems. Combination of protein and DNA biotechnology with electrochemistry has come to offer other perspectives in bioelectrochemical signal transfer between target molecules and external electrochemical circuitry based on strategic surface preparation and functional linker molecules.

The chapters in this volume offer overviews of electronic properties, electron transfer and electron-proton coupled charge transfer of biological molecules and macromolecules both in the natural aqueous solution environment and on metallic electrode surfaces, where the electrochemical potential controls biomolecular function. Redox metalloproteins and DNA-based molecules are primary targets, but amino acid and nucleobase building blocks are also addressed. Novel environments where proteins and DNA-based molecules are inserted in metallic nanoparticle hybrids or *in situ* STM configurations are other focus areas.

The chapters by Winkler *et al*. and by Wikström overview electron and electron-proton coupled charge transfer of both small electron transfer metalloproteins and large metalloenzyme complexes such as cyt *c* oxidase. A key point is the mechanistic detail now available. Percolation of electrons through the protein structure and proton hopping through conduction channels in the enzyme structures, triggered by electron transfer are important issues. Understanding of these patterns is a prerequisite for protein and enzyme voltammetry and hybrid systems for working enzyme-devices. Such perspectives are addressed by Willner and Willner, and by Butt and Armstrong. It is notable that large and fragile, sometimes multi-component enzymes can be controlled and retain close to full enzyme function at the electrochemical interface to the extent where molecular mechanisms of enzyme electrocatalysis can be mapped. This holds perspectives for multifarious technology for example in metalloenzyme biosensor function. Functional units which respond to optical, magnetic, and other signals can further be inserted between the electrode and the enzymes and biological redox chains constructed.

The chapter by Hill and Kelley addresses the interfacial electronic conductivity of DNA-based molecules controlled by the electrochemical potential. Binding of redox probes is a probe for electronic communication between the probe and the electrode through the DNA-molecular frame and therefore of the tunneling conductivity of the latter. This remains an intriguing issue as the redox-based electronic energies of the nucleobases are strongly off-resonance with the electrode Fermi energy and the redox level of the probe molecule.

Single-crystal, atomically planar electrode surfaces have paved the way for the scanning probe microscopies, STM and AFM in bioelectrochemistry. The chapter by Nichols *et al*. illuminates this powerful technology which has increased the structural resolution of the (bio)electrochemical electrode surfaces to sub-molecular levels. High-resolution images have been achieved for the biological building blocks, i.e. DNA nucleobases and amino acids, both of which form highly ordered monolayers on Au(111)- and Pt(111) - electrode surfaces. Dynamic surface phenomena such as adlayer phase transitions can also be followed. The image detail of individual molecules and patterns in their lateral organization holds clearly perspectives for understanding the interaction of biological liquids with solid surfaces.

The use of STM/AFM to biological macromolecules is discussed further in the chapters by Kuznetsov and Ulstrup, and by Zhang *et al*. Single-molecule resolution has been achieved for both redox metalloproteins and DNA-based molecules under conditions where the molecules are active in electron transfer or enzyme function. Not only structural mapping but given adequate theoretical support, electron transfer and redox enzyme function can be addressed at the single-molecule level. The Os-complexes and the redox metalloprotein, *P aeruginosa* azurin discussed in chapter 8 illuminate these perspectives which extend towards ultra-sensitive biological sensors and other "device" function. STM and in *situ* STM are theoretically demanding because the electrical current recorded does not translate directly into molecular topography. Long-range off-resonance conductivity is broadly understood in terms of electron exchange and energy gaps of appropriate atomic or molecular orbitals with exponential distance dependence of the tunneling current expected. This is sometimes observed but weak current attenuation emerges in other cases such as for single- and double-stranded oligonucleotides. This issue presently appears unsettled.

Electronic conductivity of (bio)molecules with low-lying redox states show a quite different pattern, namely two- (or multi-)step hopping through the redox state(s) induced by environmental configurational fluctuations.

Theoretical notions rest on electrochemical electron transfer but the novel environments have also disclosed new electron transfer phenomena. Switching or negative differential resistance, quite different from electrochemical electron transfer at semi-infinite electrode surfaces is immediately conspicuous. Coherent, multi-electron transfer in a single *in situ* STM event is another non-traditional electron transfer phenomenon.

(Bio)molecular electronics, enzyme electrochemistry, oligo-nucleotide organization, and high-resolution biological screening are exciting parts of new bioelectrochemistry. Networks of hybrid biomolecular structures are other novel targets. In a biotechnological perspective, fundamental bioelectrochemical innovation remains, however, essential. The objective of this volume is to illuminate these exciting new stages of bioinorganic electrochemistry.

Copenhagen and Lyngby, June 2007

Ole Hammerich, Jens Ulstrup

Chapter 1

ELECTRON TUNNELING THROUGH IRON AND COPPER PROTEINS

JAY R. WINKLER, ALEXANDER R. DUNN, CORINNA R. HESS, AND HARRY B. GRAY
Beckman Institute, MC 139-74, California Institute of Technology, Pasadena, California 91125, USA

1. INTRODUCTION

Iron and copper redox centers facilitate the transfer of electrons through proteins that are part of the respiratory and photosynthetic machinery of cells. Much work has been done with the goal of understanding the factors that control electron flow through these proteins.[1–18] The results of many of the key experiments have been interpreted in terms of semiclassical theory.

The rate of electron transfer (ET) from a donor (**D**) to an acceptor (**A**) held at fixed distance and orientation depends on of temperature (T), reaction driving force ($-\Delta G^{o}$) a nuclear reorganization parameter (λ), and an electronic coupling matrix element (H_{AB}).[4,12] The reorganization parameter reflects the changes in structure and solvation that result when an electron moves from **D** to **A**. A balance between nuclear reorganization and reaction driving force determines both the transition-state configuration and the height of the barrier associated with the ET process. At the optimum driving force ($-\Delta G^{o} = \lambda$), the reaction is activationless, and the rate (k_{ET}^{o}) is limited only by the strength of the **D**/**A** electronic coupling. When **D** and **A** are in van der Waals contact, the coupling strength is usually so large that the ET reaction is adiabatic, that is, it occurs every time the transition-state configuration is formed. In this adiabatic limit, the ET rate is independent of H_{AB} and the prefactor depends only on the frequency of motion along the reaction coordinate. An ET reaction is nonadiabatic when the **D**/**A**

O. Hammerich and J. Ulstrup (eds.), Bioinorganic Electrochemistry, 1–23.

interaction is weak and the transition state must be reached many times before an electron is transferred. The electronic coupling determines the frequency of crossing from reactants (**D** + **A**) to products ($\mathbf{D}^+ + \mathbf{A}^-$) in the region of the transition state.

The singular feature of electron transfer is that reactions can proceed at very high rates when **D** and **A** are separated by long distances. The electron tunnels through a potential barrier between **D** and **A**; for a square barrier, H_{AB} displays an exponential dependence on the distance (**R**) between the reactants.[19] The medium between redox centers potentially can control long-range ET. Owing to a 3.5–$Å^{-1}$ distance-decay constant (β), the time required for electron exchange between hydrated ferrous and ferric ions is estimated to be 5×10^{16} years if the complexes are separated by 20 Å in a vacuum.[14] Superexchange coupling via hole and electron states of the intervening medium enhances the **D**/**A** electronic interaction and produces a more gradual decrease in rate with distance. Fill the void between hydrated ferrous and ferric ions with water ($\beta = 1.59$ $Å^{-1}$)[20] and the time constant for 20–Å electron exchange decreases dramatically (400 years), but the reaction is still far too slow to support biological activity. If the distance decay factor for ET across a polypeptide is comparable to that found for electron tunneling across hydrocarbon bridges ($\beta = 0.8$–1.0 $Å^{-1}$),[14] then the time for a 20 Å electron exchange between complexed ferrous and ferric ions in the hydrophobic interior of a protein could be in the millisecond to microsecond range.

2. REORGANIZATION ENERGY

The protein fold plays a central role in lowering the reorganization energy of a biological ET reaction.[21,22] A large part of the λ-reduction results from sequestering a redox center from the aqueous solvent environment. Continuum models suggest that embedding a redox center inside a low dielectric cavity can lower the outer-sphere reorganization energy by as much as 50%.[23] Moreover, by constraining the coordination environment around metal centers, inner-sphere reorganization energy can be reduced as well.[22] Indeed, metals that are typically poor redox reagents because of large reorganization barriers can be extremely efficient when embedded in protein interiors. Copper is a case in point. The reorganization energy for electron self-exchange in $Cu(phen)_2^{2+/+}$ is ~2.4 eV; the value for Cu(II/I) in *Pseudomonas aeruginosa* azurin is 0.7 eV (*vide infra*). The 1.7 eV reduction in λ reflects the transition-state stabilization imposed by the azurin fold.[21]

Two approaches are commonly employed to estimate reorganization energies in ET reactions: the first involves driving-force variations; and the

second is based on temperature dependences. Carefully designed studies of the variation of rates with driving force can lead to reliable estimates of λ,[24–29] but there are several pitfalls. To begin with, it can be difficult to modify natural redox sites sufficiently to define λ with confidence. At low driving forces, $\ln(k_{ET})$ varies linearly with $-\Delta G^{o}$, and the slope is independent of λ. Reorganization energies extracted from these data are fraught with uncertainty because they involve the analysis of small deviations from linearity. In principle, more reliable values of λ can come from measurements at driving forces close to the reorganization energy, where rates reach a maximum and the driving-force curve flattens. Complications can arise, however, in redox processes where ET is not rate limiting. Conformationally gated reactions are a prime example of this type of behavior.[30,31]

Reorganization energies also can be extracted from studies of the temperature dependence of ET rates.[32] These would seem to be more direct and reliable than driving-force studies. The drawback, however, is that accurate λ values can be extracted only when the temperature dependence of ΔG^{o} has been determined as well.[33] In many cases, particularly with deeply buried redox sites, reduction potentials are not known with great accuracy and temperature dependences are beyond available measurement methods.

2.1 Cytochrome *c*

Early work on Ru-ammine cytochrome *c*[34,35] (104 amino acids in the horse protein; 12.5 kDa; E^{o} = 0.28 V *vs.* NHE)[36,37] included the replacement of the native Fe center with Zn.[38] Long-range ET reactions in Zn-cyt *c* were initiated by excitation of the Zn-porphyrin (ZnPor) to its long-lived (>10 ms), strongly reducing (E^{o} ~ –0.8 V *vs.* NHE) triplet excited state.[38] A driving-force study of ET rates in $Ru(NH_3)_4L$(His33)-Zn-cyt *c* (L = NH_3, pyridine, isonicotinamide) was consistent with λ_{12} = 1.2 eV.[27] Since self-exchange reorganization energies for Ru-ammine complexes (λ_{11}) are in the vicinity of 1.6 eV,[4,39] the ET kinetics suggest that λ_{22} = 0.8 eV for Zn-cyt *c*.

Studies of high-driving-force ET in heme and nonheme proteins were made possible by Ru-diimine labeling protocols and the flash-quench method.[40] The driving-force dependence of ET in $Ru(diimine)_2(im)$(His33)-Fe-cyt *c* indicates λ_{12} = 0.8 eV.[11,29] This value is lower than that found for Ru-ammine-Zn-cyt *c*, because the diimine ligands coordinated to the Ru center are larger and more hydrophobic than ammines. Consequently, the self-exchange reorganization energy for $Ru(diimine)_2(im)(His)^{3+/2+}$ is substantially smaller (λ_{11} = 0.8 eV) than that of the ammine.[4,9] The combined results from ET measurements in the Ru-ammine and Ru-diimine proteins

suggest that the reorganization energy for electron exchange between Fe(II)- and Fe(III)-cyt *c* is 0.8(1) eV.

2.2 Azurin

P. aeruginosa azurin has a Cu(II/I) reduction potential of 0.31 V *vs.* NHE.[41–43] Analysis of the driving-force dependence of Cu(I)→M(III) (M = Ru, Os) ET in M(diimine)$_2$(im)(His83)-azurin gives a reorganization energy of 0.8 eV.[44] In accord with this finding, the temperature independence (240–300 K) of Cu(I)→Ru(III) ET in Ru(bpy)$_2$(im)(His83)-azurin can be described by $\lambda_{12} = 0.7 \pm 0.1$ eV, although the observed two-fold increase in rate constant as the temperature is lowered to 170 K cannot be explained by changes in the exponential term of the semiclassical rate expression.[32] It is more likely that the Ru-Cu electronic coupling (*vide infra*) increases as the protein is cooled to 170 K.

Rates of Ru(III) and Os(III) reduction by Cu(I) have been measured in single crystals of *P. aeruginosa* M(diimine)$_2$(im)(His83)-azurin; in these cases, protein conformation and surface solvation are precisely defined by high-resolution X-ray structure determinations.[45] The time constants for electron tunneling in crystals are roughly the same as those measured in solution, indicating very similar protein structures in the two states. High-resolution structures of the oxidized (1.5 Å) and reduced (1.4 Å) forms of Ru(tpy)(bpy)(im)(His83)-azurin establish that very small changes in copper coordination accompany reduction.[45] Although Ru(bpy)$_2$(im)(His83)-azurin is less solvated in the crystal lattice, the reorganization energy for Cu(I)→Ru(III) electron transfer falls in the same range (0.6–0.8 eV) determined experimentally for the reaction in solution. It is striking that driving forces, reorganization energies, and rates of Cu(I)→M(III) (M = Ru, Os) ET are virtually unchanged when labeled azurins lose one-third of their solvent-accessible surface upon transfer from dilute solutions to crystal lattices with just 40% water.

3. ELECTRONIC COUPLING

Nonadiabatic ET reactions are characterized by weak electronic interaction between the reactants and products at the transition-state nuclear configuration ($H_{AB} \ll k_B T$). This coupling is directly related to the strength of the electronic interaction between the donor and acceptor.[46] For electron tunneling through a square potential barrier, H_{AB} drops off exponentially with increasing **D**/**A** separation.[19,47] The height of the tunneling barrier relative to the energies of the **D**/**A** states determines the distance-decay

constant (β). Hopfield estimated $\beta \sim 1.4$ Å^{-1} on the basis of measurements of the temperature dependence of ET from a cytochrome to the oxidized special pair of chlorophylls in the photosynthetic reaction center of *Chromatium vinosum*.[19] His analysis predicted that the heme edge of the cytochrome would be 8 Å from the nearest edge of the special pair (structural studies revealed that the actual distance is 12.3 Å).[48]

3.1 Superexchange Coupling

Coupling **D** to **A** through electronic interactions with the intervening bridge is called superexchange. If oxidized states of the bridge mediate the coupling, the process is referred to as "hole transfer"; mediation by reduced bridge states is known as "electron transfer". In 1961 McConnell developed a nearest-neighbor superexchange coupling model to describe charge-transfer interactions between donors and acceptors separated by spacers comprised of identical repeat units.[49] The total coupling (H_{AB}) is given as the product of the coupling-decays for each bridge site (ε). For a bridge built from identical repeat units separated by *m* bonds, H_{AB} will be proportional to ε^m. In this model, the ET rate constant will exhibit an exponential dependence on the number of bonds separating **D** and **A**.

3.2 Tunneling Pathways in Proteins

The McConnell superexchange model is too simplistic for a protein intervening medium because of the complex array of bonded and nonbonded contacts between **D** and **A**.[5,6,50–64] An important advance was made by Beratan and Onuchic, who developed a generalized tunneling pathway (TP) superexchange coupling model that reduces the diverse interactions between the atoms in a folded polypeptide to a set of three types of contacts: covalent bonds, hydrogen bonds, and through space contacts.[10,50–56] Each type of contact is assigned a coupling decay value (ε_C, ε_H, and ε_S), which permits implementation of a search algorithm for finding optimal coupling pathways through proteins. The total coupling of a single pathway is given as a product of the couplings for the individual links (expression (1-1)).[10,50–56]

$$H_{AB} \propto \Pi\varepsilon_C \Pi\varepsilon_H \Pi\varepsilon_S \qquad (1\text{-}1)$$

A tunneling pathway can be described in terms of an effective covalent tunneling path comprised of n (nonintegral) covalent bonds, with a total length equal to σ_l (expressions (1-2 and 1-3)).

$$H_{AB} \propto (\varepsilon_C)^n \tag{1-2}$$

$$\sigma_l = n \times 1.4 \text{ Å/bond} \tag{1-3}$$

The relationship between σ_l and the direct **D**-**A** distance (**R**) reflects the coupling efficiency of a pathway. The variation of ET rates with **R** is expected to depend upon the coupling decay for a single covalent bond (ε_C); the magnitude of ε_C depends critically upon the energy of the tunneling electron relative to the energies of the bridge hole and electron states.

3.3 Rate/Distance Dependence

The **D**-**A** distance decay of protein ET rate constants depends on the capacity of the polypeptide matrix to mediate distant electronic couplings. If dominant coupling pathways mediate long-range electron transfer in proteins, then single-site mutations could have profound effects on enzyme function. In addition, if single pathways operate in biological ET reactions, then they have presumably been optimized through natural selection. These consequences of tunneling pathways impart a certain lack of robustness into the protein structure/function relationship. Concerns about this issue led Dutton and coworkers to propose that a folded polypeptide matrix behaves like a glassy solvent, imposing a uniform barrier (UB) to electron tunneling.[48] Analysis of a variety of ET rates, especially those from the photosynthetic reaction center, produced a universal distance-decay constant for protein electron transfer that was in remarkable agreement with Hopfield's estimate (1.4 $Å^{-1}$).[48] Disagreements over the appropriate **D**/**A** distance measure (edge-to-edge, center-to-center) fueled disputes about whether the large body of protein ET data supports a homogeneous barrier model, or whether a structure-dependent model is necessary. Recently, the UB model has been amended to include the packing density of the protein matrix.[65] Although this model ignores bond connectivity, it does embody many of the same elements as the TP model by accounting for, in a rudimentary fashion, the protein structure dependence of long-range couplings.

The great strength of the TP model is that a straightforward analysis of a protein structure identifies residues that are important for mediating long-range coupling. Employing this model, Beratan, Betts, and Onuchic predicted in 1991 that proteins comprised largely of β-sheet structures would be more effective at mediating long-range couplings than those built from α helices.[54] This analysis can be taken a step further by comparing the coupling efficiencies of individual protein secondary structural elements

(β-sheets, α-helices). The coupling efficiency can be determined from the variation of σ_I as a function of **R**. A linear σ_I/**R** relationship implies that k_{ET}^o will be an exponential function of **R**; the distance-decay constant is determined by the slope of the σ_I/**R** plot and the value of ε_C.[12]

A β-sheet is comprised of extended polypeptide chains interconnected by hydrogen bonds; the individual strands of β-sheets define nearly linear coupling pathways along the peptide backbone spanning 3.4 Å per residue. The tunneling length for a β-strand exhibits an excellent linear correlation with β-carbon separation ($\mathbf{R}_\beta$,); the best linear fit with zero intercept yields a slope of 1.37 $\sigma_I/\mathbf{R}_\beta$ (distance-decay constant = 1.0 $Å^{-1}$). Couplings across a β-sheet depend upon the ability of hydrogen bonds to mediate the **D**/**A** interaction. The standard parameterization of the TP model defines the coupling decay across a hydrogen bond in terms of the heteroatom separation. If the two heteroatoms are separated by twice the 1.4–Å covalent-bond distance, then the hydrogen-bond decay is assigned a value equal to that of a covalent bond. Longer heteroatom separations lead to weaker predicted couplings but, as yet, there is no experimental confirmation of this relationship.

In the coiled α-helix structure a linear distance of just 1.5 Å is spanned per residue. In the absence of mediation by hydrogen bonds, σ_I is a very steep function of $\mathbf{R}_\beta$, implying that an α-helix is a poor conductor of electronic coupling (2.7 $\sigma_I/\mathbf{R}_\beta$, distance-decay constant = 1.97 $Å^{-1}$). If the hydrogen-bond networks in α-helices mediate coupling, then the Beratan-Onuchic parameterization of hydrogen-bond couplings suggests a $\sigma_I/\mathbf{R}_\beta$ ratio of 1.72 (distance-decay constant = 1.26 $Å^{-1}$). Treating hydrogen bonds as covalent bonds further reduces this ratio (1.29 $\sigma_I/\mathbf{R}_\beta$, distance-decay constant = 0.94 $Å^{-1}$). Hydrogen-bond interactions, then, will determine whether α-helices are vastly inferior to or are slightly better than β-sheets in mediating long-range electronic couplings. It is important to note that the coiled helical structure leads to poorer $\sigma_I/\mathbf{R}_\beta$ correlations, especially for values of $\mathbf{R}_\beta$ under 10 Å. In this distance region, the TP model predicts little variation in coupling efficiencies for the different secondary structures.

4. TUNNELING TIMETABLES

4.1 Ru-proteins

Plots of coupling-limited tunneling times ($1/k_{ET}^o$) *vs.* distance (**R**) are called tunneling timetables.[12–14,66] To determine the efficiency of coupling across β-sheet structures, we examined distance dependences of ET in

azurin.[67,68] The copper center in azurin is situated at one end of an eight-stranded β-barrel, ligated in a trigonal plane by two imidazoles (His46, His117) and a thiolate (Cys112); in addition, there are weak axial interactions (Met121 thioether sulfur, Gly45 carbonyl oxygen).[42,69] The azurin from *P. aeruginosa* has two additional His residues, one of which (His83) reacts readily with Ru-labeling reagents. A H83Q base mutant was prepared and individual mutant His residues were introduced at five locations on β-strands extending from the Cys112 and Met121 ligands (K122H, T124H, T126H, Q107H, M109H). Measurements of Cu(I)→ $Ru(bpy)_2(im)(HisX)^{3+}$ ET ($-\Delta G^o$ = 0.7 eV) provide a calibration for the distance dependence of electron transfer along β-strands, Fig. 1-1.

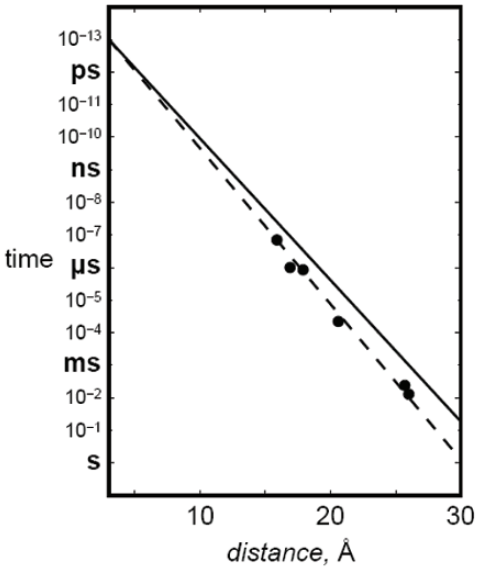

Figure 1-1. Tunneling timetable for $Ru(bpy)_2(im)(HisX)$-azurins [k_{ET}^o (X, Cu-Ru): 7.1×10^6 (122, 15.9); 2.2×10^4 (124, 20.6); 1.3×10^2 (126, 26.0); 8.5×10^5 (109, 17.9); 2.4×10^2 (107, 25.7); 1.0×10^6 s^{-1} (83, 16.9 Å)]. Solid line, β = 1.0 $Å^{-1}$; dashed line, β = 1.1 $Å^{-1}$. Adapted from ref. 13.

The driving-force-optimized electron tunneling timetable for azurin reveals a nearly perfect exponential distance dependence, with a decay constant (β) of 1.1 $Å^{-1}$, and an intercept at close contact (r_o = 3 Å) of 10^{13} s^{-1}. This decay constant is quite similar to that found for superexchange-mediated tunneling across saturated alkane bridges (β ≈ 1.0 $Å^{-1}$),[70,71] strongly indicating that a similar coupling mechanism is operative in the polypeptide.

The validity of the azurin tunneling timetable rests on the assumption that Ru-azurin structures are not very different in crystals and aqueous solutions. Our measurements of ET kinetics on crystalline samples of labeled azurins directly tested this assumption.[45] We found that the rate constants for oxidation of Cu(I) by Ru(III) and Os(III) in solutions and crystals are nearly identical for each donor-acceptor pair. It follows that the crystal structures of reduced and oxidized azurin are the relevant reactant and product states for solution ET.

It is important to distinguish between superexchange-mediated electron tunneling and multistep mechanisms that also can move charge over large molecular distances. In tunneling processes, quantum mechanical mixing of localized donor and acceptor states with oxidized (and/or reduced) bridge states couples the reactant and product states, producing an avoided crossing between the free-energy surfaces at the transition state. Importantly, oxidized (reduced) bridge states are not populated in tunneling reactions; electron transfer occurs in a single elementary reaction step. Because redox centers in metalloenzymes cannot come into close contact, electrons must tunnel between them. There is a practical upper limit to the separation distance between redox sites; if charges must be transferred farther than this range, then multiple tunneling steps are required. Long-range electron transfer can proceed by either mechanism, but each has distinct energetic and coupling requirements, and can respond quite differently to changes in reaction parameters.

The energy gap between the donor/acceptor redox levels and those of oxidized or reduced intermediate states is the primary criterion in determining when multistep tunneling becomes important (*vide infra*). In proteins with a single redox cofactor, the opportunities for multistep tunneling are limited. Extreme redox potentials are necessary to oxidize and reduce polypeptide backbones; thus multistep tunneling via backbone states will not contribute to observed ET kinetics under most solution conditions. The side chains of certain amino acids (*e.g.*, Tyr, Trp) have redox potentials that are more accessible than those of the peptide backbone.[72–76] Oxidized Trp and Tyr residues have been characterized spectroscopically in a large number of proteins, although there is a paucity of direct evidence for their involvement in multistep tunneling reactions.[77–79]

The $Ru(bpy)_2(im)(His)^{3+/2+}$ reduction potential (E^o = 1.0 V *vs.* NHE)[40] may be high enough to oxidize Trp and Tyr residues in Ru-azurin. If the reactive Cu(I) center is replaced by redox-inert Zn(II) in the protein, however, we find that photogenerated holes in $Ru(bpy)_2(im)(HisX)^{3+}$ complexes remain localized on the Ru center. The energy gap between the Ru(III) hole state and oxidized bridge states must therefore be greater than 75 meV ($3k_BT$ at 295 K). The fact that oxidized bridge states lie at higher

energy than the Ru(III) hole does not rule out multistep tunneling; endergonic steps can be compensated by favorable reactions later in a sequence. Endergonic reactions, however, become less effective as the temperature decreases, so that multistep tunneling with highly endergonic steps will exhibit a strong dependence on temperature. Our finding that the rate of Cu(I)→Ru(III) ET in $Ru(bpy)_2(im)(HisX)$-azurin is nearly independent of temperature between 240 and 300 K coupled with the observation that decreasing the temperature to 160 K produces a twofold *increase* in the ET rate demonstrate that multistep tunneling cannot explain long-range ET in Ru-azurin. Instead, the data shown in Fig. 1-1 provide a benchmark for superexchange-mediated electron tunneling in proteins.

The rates of high-driving-force ET reactions have been measured for more than 30 Ru(diimine)-labeled metalloproteins.[12,13,80,81] Only modest corrections are required to scale these rates to driving-force-optimized values, permitting comparisons of ET in different proteins. The results are summarized in the electron tunneling timetable of Fig. 1-2.

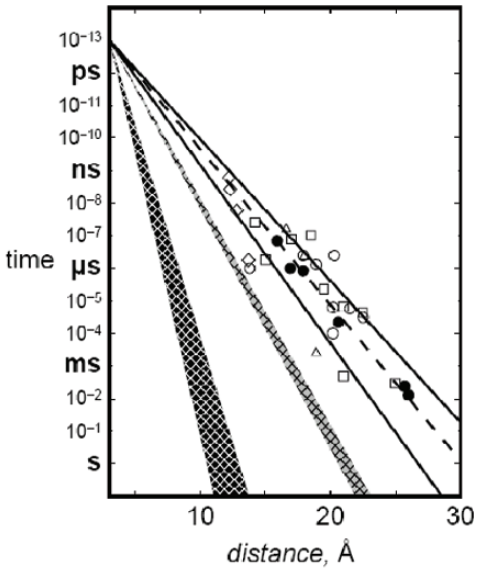

Figure 1-2. Tunneling timetable for water and Ru-modified proteins: azurin (•); cytochrome c (○); myoglobin (Δ); cytochrome b_{562} (□); and HiPIP (◊). Rates for ET reactions in crystals of tuna cytochrome *c* doped with Zn-cytochrome *c* are indicated by solid circles. The solid lines illustrate the TP predictions for coupling along β-strands ($\beta = 1.0$ Å^{-1}) and α-helices ($\beta = 1.3$ Å^{-1}); the dashed line illustrates a 1.1 Å^{-1} distance decay. Distance decay for electron tunneling through water is shown as a gray wedge. Estimated distance dependence for tunneling through vacuum is shown as the black wedge. Adapted from ref. 66.

The reported distances are all metal-to-metal measures; in the case of metal clusters, the closest metal was chosen. Tunneling times range from a few nanoseconds (12.2 Å ET in the high-potential iron sulfur protein from *C. vinosum*) to 10 milliseconds (26 Å ET in *P. aeruginosa* azurin).

The Ru-protein rates in Fig. 1-2 are scattered around the Ru-azurin $\beta = 1.1$ $Å^{-1}$ exponential distance decay. Rates at a single distance can differ by as much as a factor of 10^3 and **D/A** distances that differ by as much as 5 Å can produce virtually identical rates. Clearly, the absence of a simple exponential distance dependence in the Ru-protein rate data is a reflection of the heterogeneity of the coupling medium. The efficiency of the coupling between redox centers is determined by the three-dimensional structure of the intervening polypeptide.

4.2 Water

In 1984, Larsson suggested that long-range ET in water would be inefficient ($\beta = 2.4$ $Å^{-1}$) because of the large energy gap between the hole states of the medium and those of **D** and **A**.[82] More recent theoretical treatments, however, have produced β values in the 1.0 to 1.8 $Å^{-1}$ range.[83,84]

Investigations of $Ru(tpy)_2^{2+}$ (tpy = 2,2':6,2''-terpyridine) luminescence quenching by $Fe(OH_2)_6^{3+}$ in aqueous acidic glasses have produced a distance decay constant of 1.59 ± 0.05 $Å^{-1}$,[20,85] a value substantially larger than those for electron tunneling through saturated alkane spacers (0.9 $Å^{-1}$)[70] or proteins (1.0–1.3 $Å^{-1}$), Fig. 1-2. The region representing the distance decay for coupling through water ($\beta = 1.6$–1.7 $Å^{-1}$) demonstrates that, although better than a vacuum ($\beta = 3$–4 $Å^{-1}$), tunneling 20 Å through water is at least 100 times slower than tunneling through protein or hydrocarbon bridges. At **D**-**A** distances in the 10–Å range, however, ET reactions mediated by intervening water bridges could be key steps in the catalytic cycles of certain redox enzymes.[86]

5. ELECTRON TUNNELING WIRES

5.1 Ru-Wires for Cytochrome $P450_{cam}$

The original impetus for the construction of substrates linked to photoredox units was the desire to observe the fleeting intermediates in P450 catalysis, Fig. 1-3.[87–89] Under biological conditions the rate determining step (RDS) in catalysis is the addition of a second electron to the dioxygen-bound

ferrous heme by the enzyme putidaredoxin (putd). Subsequent catalytic events occur far too rapidly to be observed under normal conditions.

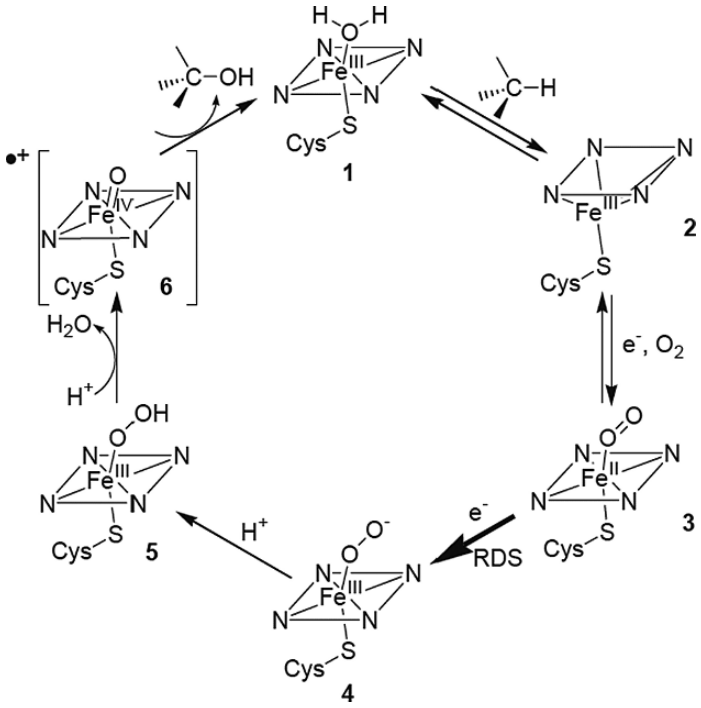

Figure 1-3. The cytochrome $P450_{cam}$ catalytic cycle. Upon binding, the substrate displaces water, converting the heme from six-coordinate, low-spin (**1**) to five-coordinate, high-spin (**2**). Subsequent reduction by putd produces a ferrous heme, which binds dioxygen (**3**). Reduction of **3** produces a ferrous, peroxide-bound heme (**4**), which rapidly protonates (**5**). In the prevalent model, the peroxide then undergoes heterolysis to produce water and a ferryl $[Fe(IV)=O]^{\bullet+}$ species (compound I, **6**), which oxidizes the substrate. See refs. 87–89.

In order to observe intermediates **5** and **6**, we have sought to use ruthenium tris-bipyridyl complexes linked to $P450_{cam}$ substrates or heme ligands (Ru-wires) to photochemically reduce **3**, thus replacing the sluggish reduction by putd with a rapid photochemical trigger. The Ru-wires investigated consist of a Ru-diimine moiety connected to adamantane, imidazole, or ethylbenzene by either an alkyl[90] or perfluorobiphenyl[91] bridge, Fig. 1-4. The Ru-wires bind $P450_{cam}$ with micromolar K_d's, as evidenced by energy transfer from the Ru-diimine excited state to the heme, and changes to the heme absorption spectrum, Table 1-1.

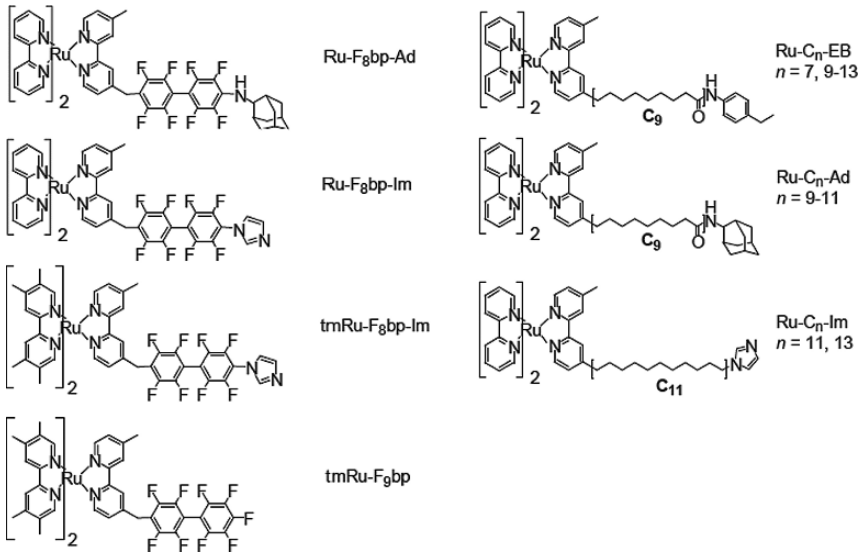

Figure 1-4. Ru-wires. Variation of the linkage connecting the Ru-diimine to the enzyme substrate or heme ligand modifies the electronic coupling and hence the rate of electron transfer. The tetramethylated ancillary bipyridine ligands in tmRu-F_8bp-Im and tmRu-F_9bp decrease the reduction potential of the excited Ru-diimine by ~130 mV. See ref. 91.

Interestingly, neither adamantyl nor imidazole is necessary for binding: Ru-wires terminating in either an alkyl chain or a perfluorobiphenyl bind to the enzyme. This observation suggests that interactions of the protein with the Ru-diimine and linker moieties provide the bulk of the binding energy.

The Ru-heme distances for a series of ethylbenzene Ru-wires remain roughly constant with varying alkyl chain lengths, Table 1-1,[92] indicating that an optimal Ru-heme distance exists in the Ru-wire:P450 conjugate. In contrast, Ru-C_{13}-Im binds $P450_{cam}$ (K_d = 4.1 μM), while Ru-C_{11}-Im does not. Evidently, the imidazole tip must ligate the heme iron in order for binding to occur, suggesting a substantial energetic penalty for its sequestration in the hydrophobic P450 active site. This result demonstrates that sensitive binding discrimination is possible with properly designed probe molecules. The Δ and Λ isomers of Ru-C_9-Ad bind $P450_{cam}$ with similar dissociation constants ($K_d(\Delta)$ = 190 nM; $K_d(\Lambda)$ = 90 nM), corresponding to a difference in binding energies of 0.46 kcal mol^{-1}.[93] Detailed analysis shows that the apparent K_d for the racemate is not the average of the stereoisomer K_d's.[94]

Photogenerated reduced or oxidized alkyl Ru-wires transfer electrons or holes to the $P450_{cam}$ ferric heme with time constants of around 50 ms, Fig. 1-5.

Table 1-1. Ru-wire dissociation constants and Ru-Fe distances derived from FET measurements.

Compound	K_d, **μM**	**Ru-Fe, Å**
Ru-C_{13}-EB	1.7 ± 0.4	20.6 ± 0.2
Ru-C_{12}-EB	1.5 ± 0.3	20.5 ± 0.2
Ru-C_{11}-EB	0.9 ± 0.4	20.1 ± 0.3
Ru-C_{10}-EB	0.9 ± 0.4	19.9 ± 0.1
Ru-C_9-EB	0.7 ± 0.1	19.4 ± 0.1
Ru-C_7-EB	6.5 ± 1.3	19.5 ± 0.1
Ru-C_9-Ad	0.8 ± 0.3	21.0 ± 0.3
Ru-C_{11}-Ad	0.7 ± 0.2	21.4 ± 0.2
Ru-C_{13}-Im	4.1 ± 1.1	21.2 ± 0.1
Ru-C_{11}-Im	>50	NA
Ru-F_8bp-Ad	0.08 ± 0.01	22.1
Ru-F_8bp-Im	3.7 ± 0.5	18.1[a]
Ru-F_8bp-Im	0.48 ± 0.18	18.1
Ru-F_9bp	2.1 ± 1.3	17.0

[a]In accord with the Ru-Fe distance calculated for tmRu-F_8bp-Im.

These rates are typical for ET through saturated bonds over comparable distances. In contrast, Ru-F_8bp-Im and tmRu-F_8bp-Im reduce the ferric heme directly from the excited state, Fig. 1-6. In particular, tmRu-F_8bp-Im photoreduces $P450_{cam}$ with a time constant of ~40 ns, five orders of magnitude faster than putd.

Our results demonstrate that it is possible to trigger reactions in the buried active sites of proteins on micro- to nanosecond timescales. In particular, the direct photoreduction observed with tmRu-F_8bp-Im occurs on timescales that cannot be accessed using stopped-flow techniques. The preassociation of the Ru-wire and the enzyme also circumvents the time limits otherwise imposed by diffusion.

Ru-wires allow the ET pathway between the Ru-diimine and the heme to be altered while retaining the surrounding protein matrix. Ru-wire:$P450_{cam}$ conjugates thus serve as a useful complement to synthetic[70,95–100] and protein[12,13] ET systems.

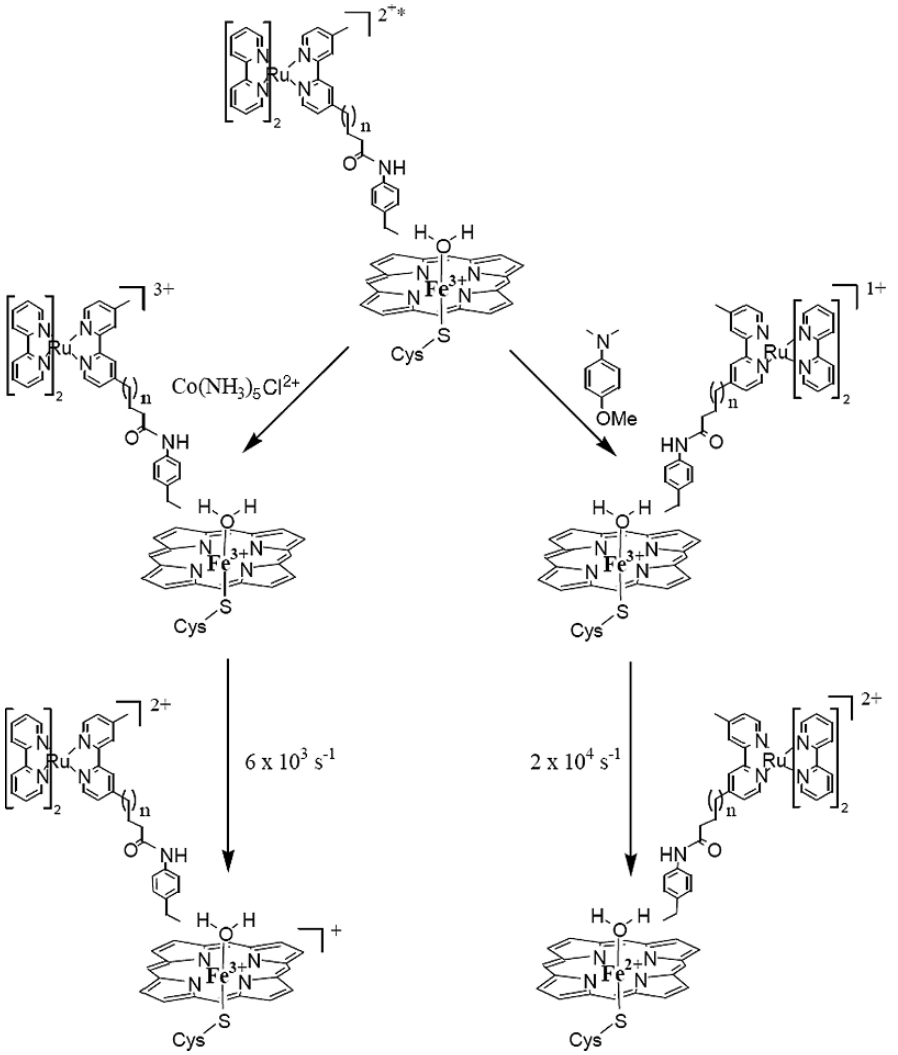

Figure 1-5. The flash-quench sequence for delivering electrons or holes to the active site of $P450_{cam}$. The Ru-wire is excited with 470-nm light (Ru*), and intercepted with either $Co(NH_3)_5Cl^{2+}$ or *p*-methoxy-*N*,*N*-dimethylaniline (PMDA) to generate the oxidized (Ru^{3+}) or reduced (Ru^{+}) Ru-wire. The photochemically generated hole or electron tunnels to the heme on the millisecond timescale, forming a heme cation radical or ferrous heme. See ref. 90.

ET through the perfluorobiphenyl bridge is 1500 times faster than through the alkyl chain, demonstrating that the nature of the intervening medium clearly mediates **D-A** coupling. Phototriggered ET is not observed in the tmRu-F_9bp and Ru-F_8bp-Ad:$P450_{cam}$ conjugates, again confirming the importance of the intervening pathway.

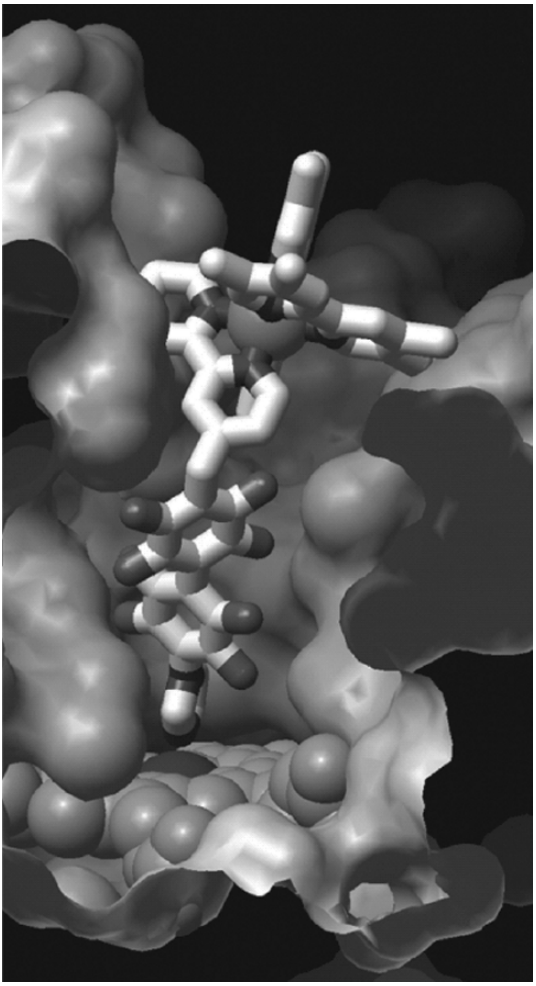

Figure 1-6. Structural model of tmRu-F_8bp-Im bound in the active site of $P450_{cam}$. The perfluorobiphenyl bridge couples $*Ru^{2+}(L_2)L'$ to the heme, facilitating direct photoreduction ($-\Delta G^o \sim 0.45$ eV) with a time constant of 36 ns. Adapted from ref. 91.

Kurnikov has calculated molecular trajectories for Ru-wire docking in the $P450_{cam}$ active-site channel using molecular dynamics methods.[101] The couplings mediated by a perfluorobiphenyl bridge are dominated by superexchange through extra electron states, while those through hydrocarbon bridges are dominated by hole-mediated superexchange interactions. An important finding is that a small number of wire conformations with strong donor-acceptor couplings can account for the

rapid ET rates in the Ru-wire:$P450_{cam}$ conjugates. Unusually rapid wire to heme ET in conjugates of inducible nitric oxide synthase with Re(perfluorobiphenyl)-wires[102] also has been observed.[103]

$P450_{cam}$ hydroxylates Ru-C_9-Ad when supplied with electrons via the natural NADH/putidaredoxin reductase/putd reduction relay.[104] Ru-C_9-Ad hydroxylation occurs at only 1.6% the rate of camphor hydroxylation, and only 10% of the electrons supplied by NADH go to product formation. Presumably the rest are diverted to the formation of reduced oxygen species such as superoxide or hydrogen peroxide.[105] The remarkable ability of $P450_{cam}$ to hydroxylate a molecule so structurally different from camphor supports the hypothesis that the structural flexibility inherent in the P450 fold allows these enzymes to hydroxylate structurally diverse substrates.[106,107]

5.2 Amine Oxidase

The conversion of amines to aldehydes and ammonia takes place at an amine oxidase (AO) active site that contains both copper and topaquinone (TPQ) cofactors.[108–111] The role of copper (if any) in catalysis remains a matter of debate.[112] The reduction potentials of the deeply buried TPQ and copper cannot be accurately measured using conventional electrochemical techniques. Instead, we measured the TPQ potential using gold electrodes functionalized with a phenyl-alkynyl bridge (DEA-OPE-SH, Fig. 1-8)[113] designed to bind in the active site of the *Arthrobacter globiformis* enzyme (AGAO),[114] thus providing an ET conduit from the electrode to the TPQ, Figs. 1-7 and 1-8. The TPQ potential was found to be –140 mV *vs.* SCE (phosphate, pH 7),[113] in accord with those of quinone model complexes.[115] Addition of the AGAO substrate phenethylamine quenches the electrochemical response, indicating that the DEA-OPE-SH bridge binds in the active site.

The TPQ reduction potential shows a linear variation with pH of –60 mV/pH, indicating a $2e^-,2H^+$ ET process, in contrast to the $2e^-,3H^+$ ET observed with model compounds.[113] Presumably the protein matrix or nearby Cu(II) stabilizes the deprotonated topaquinol. No copper electrochemistry was observed. It is not clear whether the copper potential is anomalously low or if it could not be measured due to weak electronic coupling with the phenyl-alkynyl bridge.

A distance decay constant of ~0.5 $Å^{-1}$ has been extracted from work on phenyl-ethynyl oligiomers.[98,116] In accord with this value, the CVs obtained at scan rates up to 1 V s^{-1} place a lower limit of 10^3 s^{-1} for tunneling to TPQ through the 22 Å wire; the corresponding rates through protein (1.1 $Å^{-1}$)[12,13] and water (1.6 $Å^{-1}$)[20] would be about 3 and 10^{-4} s^{-1}. It is very likely,

therefore, that the DEA-wire is the coupling element between the gold electrode and TPQ, and, importantly, that tunneling timetables can play a key role in the design of functionalized electrodes for redox-active enzymes.

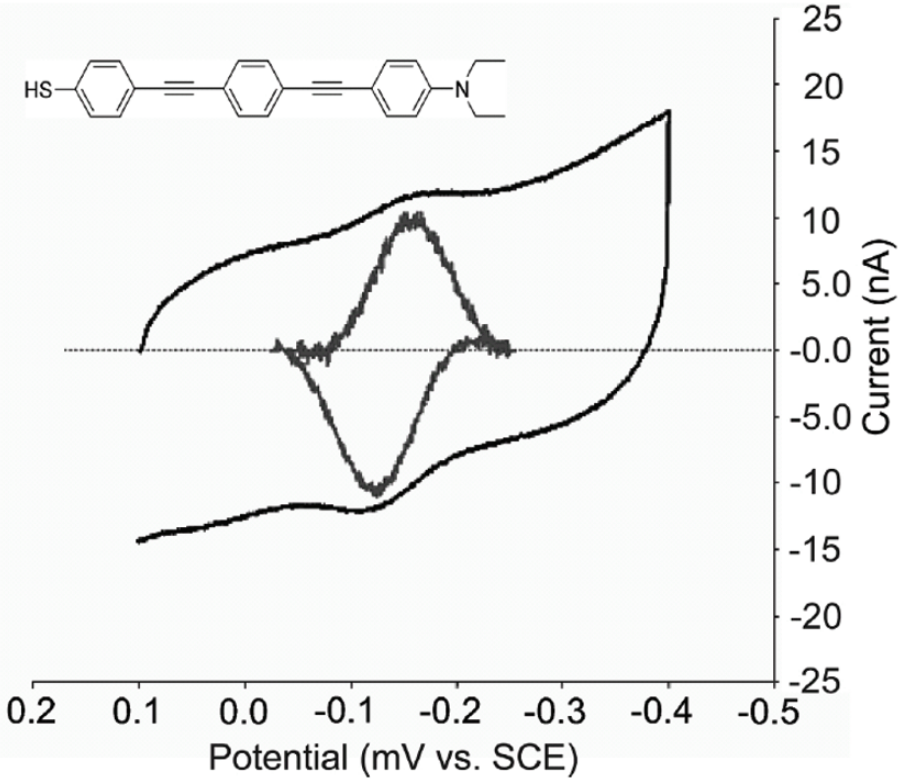

Figure 1-7. (Inset) DEA-OPE-SH. CV (black) and background-subtracted voltammogram (gray; not to scale) for AGAO on Au-bead electrodes modified with DEA-OPE-SH in 10 mM potassium phosphate, pH 7 (scan rate 100 mV s^{-1}). Gold-bead electrodes were soaked in mM solutions of DEA-OPE-SH for 24 h. Reductive stripping analyses of the resulting films indicated ~70% coverage. The modified electrodes were then incubated with AGAO for 24–48 h to allow binding to the adsorbed wires. Adapted from ref. 113.